

Equation of state and shock compression of warm dense sodium – a first-principles study

Shuai Zhang,^{1, a)} Kevin P. Driver,¹ François Soubiran,¹ and Burkhard Militzer^{1, 2, b)}

¹⁾Department of Earth and Planetary Science, University of California, Berkeley, California 94720, USA

²⁾Department of Astronomy, University of California, Berkeley, California 94720, USA

(Dated: 14 July 2018)

As one of the simple alkali metals, sodium has been of fundamental interest for shock physics experiments, but knowledge of its equation of state (EOS) in hot, dense regimes is not well known. By combining path integral Monte Carlo (PIMC) results for partially-ionized states [B. Militzer and K. P. Driver, Phys. Rev. Lett. **115**, 176403 (2015)] at high temperatures and density functional theory molecular dynamics (DFT-MD) results at lower temperatures, we have constructed a coherent equation of state for sodium over a wide density-temperature range of $1.93 - 11.60 \text{ g/cm}^3$ and $10^3 - 1.29 \times 10^8 \text{ K}$. We find that a localized, Hartree-Fock nodal structure in PIMC yields pressures and internal energies that are consistent with DFT-MD at intermediate temperatures of $2 \times 10^6 \text{ K}$. Since PIMC and DFT-MD provide a first-principles treatment of electron shell and excitation effects, we are able to identify two compression maxima in the shock Hugoniot curve corresponding to *K*-shell and *L*-shell ionization. Our Hugoniot curves provide a benchmark for widely-used EOS models, SESAME, LEOS, and Purgatorio. Due to the low ambient density, sodium has an unusually high first compression maximum along the shock Hugoniot curve. At beyond 10^7 K , we show that the radiation effect leads to very high compression along the Hugoniot curve, surpassing relativistic corrections, and observe an increasing deviation of the shock and particle velocities from a linear relation. We also compute the temperature-density dependence of thermal and pressure ionization processes.

I. INTRODUCTION

The behavior of sodium and other alkali metals at extreme conditions has generated intense scientific interest over many decades as experimental and theoretical technology has evolved to facilitate studies of increasingly atypical states. At ambient conditions, sodium has long been known as a prototypical, simple, free-electron metal¹ with a high-symmetry, bulk-centered cubic (bcc) structure. Recent interest in sodium has been driven by the ability to carefully probe exotic high-pressure states², made possible by improvements in static-compression^{3,4} and single-crystal experimental techniques⁵. A number of experimental and theoretical works have revealed that sodium exhibits anomalous structural⁵⁻¹¹, electronic and optical^{9,12-21}, and melting^{16,22-27} behavior at high pressure. Among the structural studies, high-pressure X-ray diffraction experiments have explored sodium up to pressures and temperatures of 150 GPa and 1000 K, observing a complex series of phase transitions^{5,8,10} from the bcc phase to at least seven lower-symmetry phases. Sodium also displays an anomalous melting curve maximum²² in this pressure range as the liquid undergoes structural electronic changes, becoming more dense than the solid over a large pressure range of $\sim 60 \text{ GPa}$. At even higher pressures, beyond 200 GPa, sodium undergoes a metal-insulator

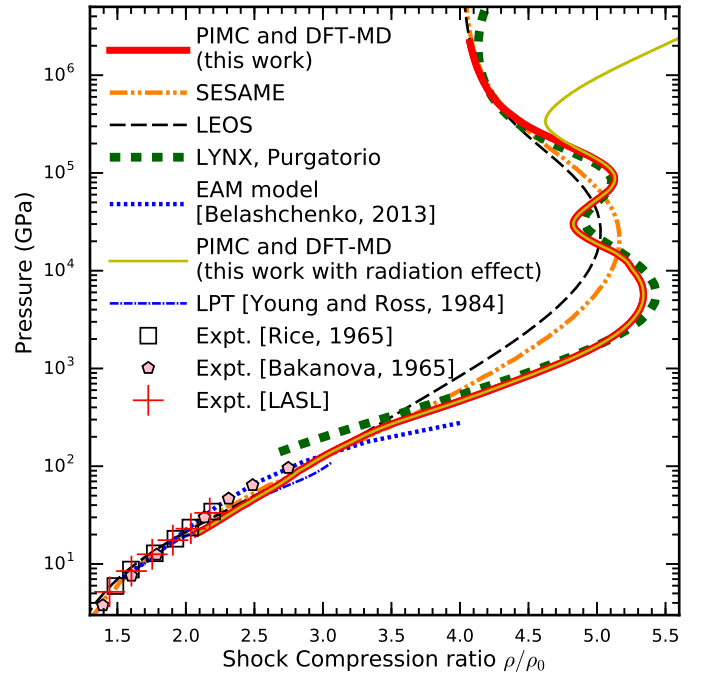


FIG. 1. Principal Hugoniot of Na obtained in this work in comparison with that considering the photon radiation correction and those from SESAME, LEOS, and Purgatorio (Lynx) models.

^{a)}Electronic mail: shuai.zhang01@berkeley.edu

^{b)}Electronic mail: militzer@berkeley.edu

transition¹² by forming an electrider²⁰. *Ab initio* random structure searches predict that sodium will ultimately become a reentrant metal at a pressure of 15.5 TPa at 0

K²⁸.

Analogous to the impact that improved static-compression technology has had for alkali metals in the condensed matter regime, we can expect future dynamic compression research to routinely probe the gigabar (Gbar)^{29,30} pressures and provide new data on the behavior of warm dense matter (WDM). Shock measurements of hot, dense alkali metals are expected to be an important component of solving problems in astrophysics, planetary physics, stockpile stewardship, and inertial fusion. Thus far, only relatively low pressure ($P < 228$ GPa³¹, $T < 8168$ K) shock experiments have been performed on sodium. Early dynamic compression experiments were motivated by compressibility of metals and the simplicity of ambient sodium as a material for the study of fundamental shock physics behavior^{32–34}. More recent shock experiments have been motivated by the prospect of observing the metal-insulator transition³¹.

Complementary to the shock experiments, there have been a number of theoretical works aiming at calculating the equation of state (EOS) and shock Hugoniot curve using either analytic approaches^{35,36} or semi-classical free-energy models^{37–39}, fluid-variational theory⁴⁰, local pseudopotential theory⁴¹, or EAM potentials^{42–44}. While each of these methods agrees reasonably well with the available low-pressure shock Hugoniot data ($P < 100$ GPa), none possess the rigor that is necessary to treat the strong coupling, quantum degeneracy, and ionization physics associated with hot, dense plasma regimes, that Gbar-shock experiments will access.

Development of rigorous, first-principles frameworks, such as path integral Monte Carlo (PIMC)^{45–47} or density functional theory molecular dynamics (DFT-MD)^{48–51}, for computing the EOS and behavior of materials in extreme pressure and temperature conditions is needed as Gbar-range shock experiments are emerging and data need to be interpreted. Recently, we have been developing PIMC for simulating heavier elements^{46–48,52–58}, which is efficient at high temperatures, and can be used to complement DFT-MD calculations that are efficient at comparatively low temperatures. Combined data from PIMC and DFT-MD provide a coherent EOS over a wide density-temperature range that spans the condensed matter, WDM, and plasma regimes. In the current work, we use PIMC and DFT-MD to compute the EOS, shock compression behavior, and plasma structure evolution of sodium across a much larger density-temperature range than has ever been studied in experiments or in theory. We provide our EOS table and shock Hugoniot curve as a theoretical benchmark in comparison with widely-used EOS database models and experiments.

The paper is organized as follows: Section II discusses details of our PIMC and DFT-MD simulation methods. In Sec. III, we discuss several results: (1) comparison of the performance of different choices for PIMC nodal surfaces, (2) the internal energies and pressures, (3) shock Hugoniot curves, and (4) the density-temperature evolution of ionization processes. Finally, in Sec. IV, we

conclude.

II. SIMULATION METHODS

A reliable theoretical scheme for simulating materials across a wide range of density and temperature conditions naturally involves treating physics appropriately in different regimes. In the limit of high temperature (above 10^8 K), materials tend to behave as weakly-interacting plasmas because of strong thermal ionization. Under such conditions, the ideal Fermi gas model and the Debye-Hückel theory⁵⁹ are good approximations. At low to intermediate temperatures ($T < 10^6$ K), standard, orbital-based, Kohn-Sham DFT-MD is a suitable option to derive the EOS because it fully accounts the bonding effects and bound states within certain approximations of the exchange-correlation functional. However, the need to explicitly compute all partially occupied electronic orbitals causes DFT-MD to become computationally intractable beyond temperatures of roughly 10^6 K. Recent work on orbital-free DFT^{48,50,60,61} and extended DFT-MD with free electron approximation for high energies⁵¹ have made progress toward overcoming this difficulty, but their general applicability and accuracy needs to be further examined.

PIMC simulates all quantum, many-body exchange and correlations effects and provides the most natural formulation to compute accurate EOSs at high temperatures ($T > 10^6$ K). In PIMC, the thermal density matrix is expressed as Feynman path integral⁶², which treats electrons and nuclei as quantum paths that are cyclic in the imaginary time $0 \leq t \leq \beta = 1/k_B T$, where k_B is the Boltzmann constant. Therefore, PIMC becomes increasingly efficient at higher temperatures as paths become shorter and more classical in nature. However, application of PIMC to study real materials other than hydrogen^{45,52,63–69}, helium^{53,70}, hydrogen-helium mixtures⁷¹, and one-component plasmas^{72,73}, is difficult because of the complex fermion sign problem, nonlocal pseudopotentials, and complex nodal structures⁷⁴.

The sign problem in fermionic PIMC simulations is usually addressed with the fixed-node approximation⁷⁴ that restricts paths to positive regions of a trial density matrix, $\rho_T(\mathbf{R}, \mathbf{R}_t; t) > 0$. The restricted path integral reads,

$$\rho_F(\mathbf{R}, \mathbf{R}'; \beta) = \frac{1}{N!} \sum_{\mathcal{P}} (-1)^{\mathcal{P}} \int_{\mathbf{R} \rightarrow \mathcal{P}\mathbf{R}', \rho_T > 0} d\mathbf{R}_t e^{-S[\mathbf{R}_t]}, \quad (1)$$

where \mathcal{P} denotes permutations of identical particles, and S is the action that weights the paths. The most common approximation to the trial density matrix is a Slater determinant of single-particle density matrices,

$$\rho_T(\mathbf{R}, \mathbf{R}'; \beta) = \left\| \rho^{[1]}(\mathbf{r}_i, \mathbf{r}'_j; \beta) \right\|_{ij}, \quad (2)$$

in combination with the free-particle (FP) density ma-

trix,

$$\rho_0^{[1]}(\mathbf{r}, \mathbf{r}'; \beta) = \sum_{\mathbf{k}} e^{-\beta E_{\mathbf{k}}} \Psi_{\mathbf{k}}(\mathbf{r}) \Psi_{\mathbf{k}}^*(\mathbf{r}'), \quad (3)$$

which represents a sum over all plane waves $\Psi_{\mathbf{k}}(\mathbf{r})$ with energy $E_{\mathbf{k}}$.

PIMC with FP nodes gives exact results in the limit of high temperature⁵³. Developments of this method have allowed for remarkable progress. Using FP nodes, we have successfully obtained the EOS of several heavy elements (C⁴⁶, N⁵⁷, O⁵⁶, Ne⁵⁵) and compounds (H₂O⁴⁶). The combined results of PIMC and DFT-MD have bridged the WDM gap between DFT-MD and the high temperature limit and provided consistent sets of coherent EOS from first principles.

Several attempts have been made to go beyond FP nodes in PIMC simulations^{66,75}. In recent work⁴⁷, we show that the applicability range of PIMC simulations can extend to lower temperatures when a number of n_s atomic orbitals at each ion I are added to the FP nodes,

$$\rho^{[1]}(\mathbf{r}, \mathbf{r}', \beta) = \rho_0^{[1]}(\mathbf{r}, \mathbf{r}'; \beta) + \sum_{I=1}^N \sum_{s=0}^{n_s} e^{-\beta E_s} \Psi_s(\mathbf{r} - \mathbf{R}_I) \Psi_s^*(\mathbf{r}' - \mathbf{R}_I). \quad (4)$$

Our results for a single silicon atom in periodic boundary condition showed that nodes derived from Hartree-Fock (HF) orbitals yield highly accurate predictions for the pressure and the internal energy at much lower temperature than is accessible with FP nodes. The combined results using this PIMC method and DFT-MD provided a coherent EOS for dense silicon plasmas over a wide density-temperature grid (2.3-18.6 g/cm³, 5×10^5 - 1.3×10^8 K). In this work, we will also investigate the effects of various nodal surfaces in PIMC calculations and show that the localized, Hartree-Fock orbitals yield accurate pressures and internal energies for sodium.

Our PIMC simulations are performed within the fixed node approximation⁷⁴ and based on the CUPID code⁷⁶. Similar to the PIMC simulations of Si⁴⁷ and recently of Na at one density⁵⁸, we treat the nuclei classically because of the high temperatures considered here. Electronic Coulomb interactions are introduced via pair density matrices⁷⁷.

DFT-MD simulations use the Vienna *Ab initio* Simulation Package (VASP)⁷⁸ and implement exchange-correlation functionals within the local density approximation (LDA)^{79,80}. The effect of using other forms of exchange-correlation functionals is small, in comparison to the effects of thermal excitations, as will be discussed in Sec. III A. We use a projected augmented wave (PAW) pseudopotential⁸¹ with a frozen, 1s² electrons core and a small core radius of 1.45 Bohr, which is the hardest one available for Na in VASP⁸².

Since the width of the electronic bands is small compared to the thermal excitation energies, we use the Γ

point for sampling the Brillouin zone. We choose plane wave basis with a large cutoff of 4000 eV to account for the electrons that are excited to the very high-energy states. We use a time step of 0.2 fs and perform DFT-MD simulations typically for over 2000 steps. A large number of temperature, energy, and pressure fluctuations are observed, which indicate the simulations have reached equilibrium. We discard 20% of the trajectories at the beginning and average the internal energy and pressure to derive the EOS. In order to put the PAW-LDA pseudopotential energies on the same scale as all-electron calculations, we shifted all of our VASP DFT-MD energies by -161.3386 Ha/atom. This shift was determined by performing isolated, all-electron atomic calculations with the OPIUM code⁸³ and corresponding isolated-atom calculations in VASP.

Most of our simulations start from a bcc cell with 8 atoms. In comparison with using a 54-atom cell, DFT-MD simulations with the 8-atom cell is sufficient in providing well converged internal energies and pressures down to temperatures below 5.0×10^4 K. For example, the difference is 0.1 eV/atom in internal energy and 0.3 GPa in pressure between simulations using an 8- and a 54-atom cells, at 3.87 g/cm³ and 5.05×10^4 K. At lower temperatures, the system could tend to freeze and is subject to larger finite-size errors. In order to maximally eliminate this effect, we use a larger, 54-atom cell at these temperatures up to 2.0×10^5 K, as long as the computational cost is affordable. We simulate data along nine isochores corresponding to 2-, 3-, 4-, 5-, 6-, 7-, 8-, 10-, and 12-fold compression of ambient density $\rho_{\text{ambient}} = 0.96663$ g/cm³. For each density, we study the temperature range from 10^3 to 1.29×10^8 K, relevant to the regime of WDM and stellar interiors (Figs. 1-2).

III. RESULTS

A. Comparison of PIMC methods

In Ref. 47, we have shown that accuracy of PIMC simulations can be improved by introducing atomic orbitals, derived with the HF method, to the fermion nodes. Here we investigate whether any further improvement can be made by representing the orbitals with more accurate basis sets, including a large number of localized orbitals or by deriving the orbitals with LDA or generalized gradient approximation in the Perdew-Burke-Ernzerhof (PBE) type⁸⁶, instead of HF. Before performing many-atom simulations, we tested various methods of introducing atomic orbitals to study one stationary sodium atom in a periodic 5-Bohr cubic box, and compared the results in Fig. 3 and Table I.

Figure 3 shows the difference in internal energy and pressure between PIMC and DFT-MD calculations. At temperatures of $T > 2 \times 10^6$ K, all PIMC energies and pressures are systematically higher than our DFT-MD results within LDA or PBE. This can be attributed to the

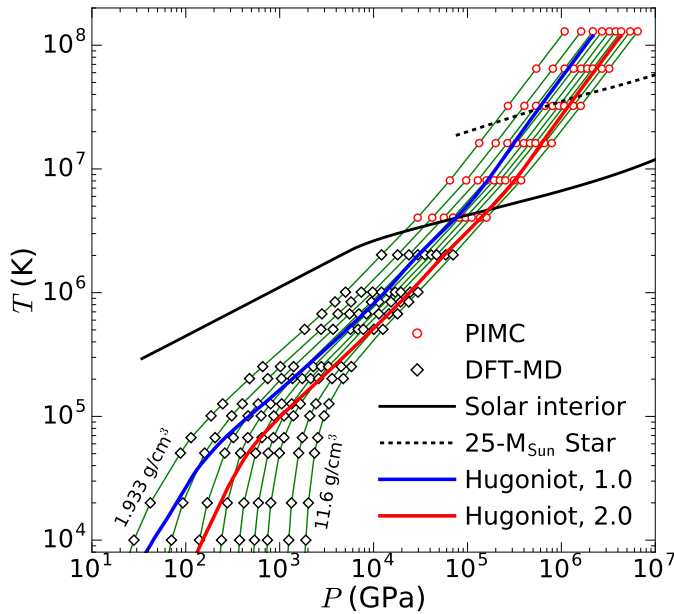


FIG. 2. Nine isochores (corresponding to 2-12 ρ_{ambient}) in a temperature-pressure plot, along with the interior profiles of the Sun⁸⁴ and a star at the end of its helium burning⁸⁵. The $P-T$ conditions of our PIMC and DFT-MD simulations and two Hugoniot curves with initial densities ρ_0 of 1.0 and 2.0 times the ambient density are also shown.

excitations of 1s electrons, which are treated explicitly as the other outer-shell electrons in PIMC, but are frozen in the pseudopotential of DFT-MD calculations.

At temperatures of $T \leq 2 \times 10^6$ K, the energies from PIMC computations with FP nodes are systematically too high, while the pressures remain quite reasonable. In contrast, using PIMC with HF nodes, the results are in much better agreement with PBE predictions. This suggests that FP nodes do not lead to the correct K and L shell structures of the atom, which is primarily a local property, so the error in the energy does not depend significantly on density. At $T < 10^6$ K, pressures from our PIMC+13 HF simulations are high, so are the uncertainties. This is due to the low sampling efficiency of PIMC at these temperatures.

Table I lists additional PIMC results for two temperatures of 1 and 2 million Kelvin. In all cases, the orbitals were derived with spin-restricted GAMESS⁸⁷ calculations of the Na^+ ion so that we can use the same orbitals for both spin channels in PIMC calculations. This is a reasonable approximation because the spin state is of minor importance at high temperatures. This is confirmed by DFT-MD calculations: within LDA and PBE, the spin-polarized (5+6) and spin-unpolarized calculations yield similar results for the temperature range under consideration.

In our PIMC calculations with localized nodal surfaces, we need a minimum of 6 atomic orbitals to provide at least one bound state for every electron. Table I shows

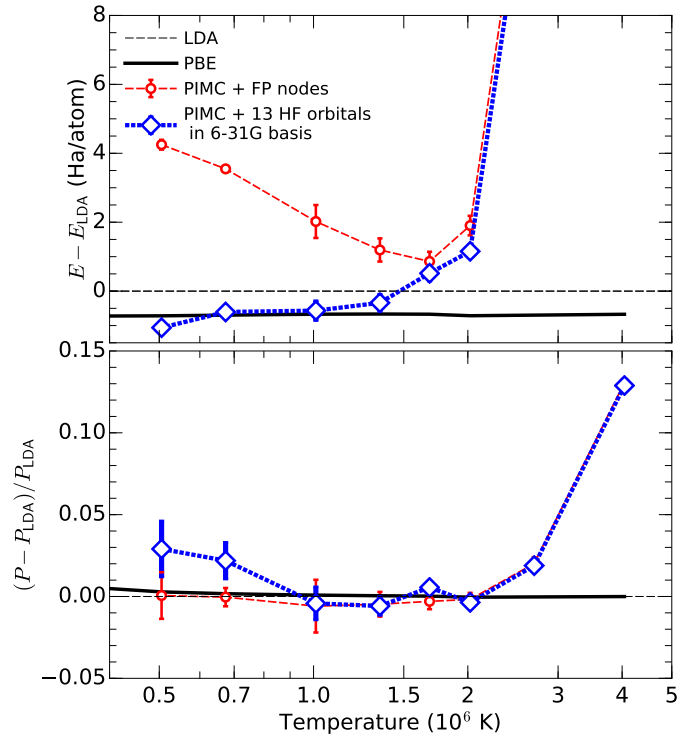


FIG. 3. Differences in internal energies and pressures of a single Na atom in a periodic 5-Bohr cubic cell calculated using different methods relative to those within local density approximation (LDA). Dark solid lines represent DFT results obtained with the Perdew-Burke-Ernzerhof (PBE) functional. Colored dashed lines represent PIMC results with free-particle and Hartree-Fock nodes. The LDA and PBE calculations do not include any excitation of the 1s electrons, which explains the deviations from the PIMC results for $T > 2 \times 10^6$ K.

TABLE I. Comparison of energies and pressures calculated using different methods. For the PIMC calculations, we also specify the node type, the basis of localized orbitals and their numbers n_s . The internal energies are in units of Ha/atom, pressures are in GPa.

Method	Basis	n_s	E	σ_E	$E - E_{LDA}$	P	σ_P	$P - P_{LDA}$
$T=2020958$ K								
LDA			-60.61			11354.6		
PBE			-61.32		-0.71	11349.6		-4.9
PIMC-FP		0	-58.67	0.46	1.93	11356.4	68.1	1.8
PIMC-HF	6-31G	6	-59.06	0.37	1.55	11357.7	56.0	3.1
PIMC-HF	6-31G	13	-59.45	0.19	1.16	11313.6	29.7	-41.0
PIMC-HF	6-31+G	13	-59.15	0.27	1.46	11362.1	42.6	7.5
PIMC-HF	6-31+G	17	-59.13	0.31	1.48	11360.8	49.3	6.2
PIMC-LDA	6-31G	13	-59.77	0.43	0.83	11283.4	66.3	-71.2
PIMC-PBE	6-31G	13	-59.28	0.34	1.32	11340.0	53.0	-14.6
PIMC-PBEX	6-31G	13	-58.92	0.39	1.69	11405.4	59.9	50.8
$T=1010479$ K								
LDA			-112.87	0.00	0.00	4528.0	0.0	0.0
PBE			-113.54	0.00	-0.67	4531.8	0.0	3.8
PIMC-FP		0	-111.14	0.80	1.73	4474.0	125.2	-54.0
PIMC-HF	6-31G	6	-113.12	0.33	-0.24	4544.7	51.5	16.7
PIMC-HF	6-31G	13	-113.44	0.29	-0.57	4508.9	45.8	-19.1
PIMC-HF	6-31+G	13	-113.47	0.23	-0.60	4508.2	37.0	-19.8
PIMC-HF	6-31+G	17	-112.73	0.31	0.15	4627.1	49.9	99.1
PIMC-LDA	6-31G	13	-113.53	0.36	-0.65	4473.6	55.7	-54.4
PIMC-PBE	6-31G	13	-113.67	0.32	-0.80	4466.6	52.6	-61.4
PIMC-PBEX	6-31G	13	-113.38	0.32	-0.51	4507.5	50.8	-20.5

that we found no statistically significant difference between using 6 and 13 HF orbitals in PIMC calculations, for both temperatures. At 1010479 K, the PIMC pressure and energy become too high when we increase the number of orbitals to 17. We attribute this deviation to our small simulation cell of 5.0 Bohr. The highest atomic orbitals are too delocalized to fit into this cell.

We find no statistically significant differences in the PIMC results between using a 6-31G and a slightly more accurate 6-31+G basis set. Both yield similar HF energies that are 0.176 Ha higher than basis set-converged HF calculations with a TZV basis. This difference is within the error bar of typical PIMC calculations.

We also test whether there would be an advantage in deriving the atomic orbitals with LDA or PBE methods rather than with HF theory, and find no significant difference. Furthermore, our studies with orbitals that are derived with just PBE exchange (PBEX) lead to similar PIMC results.

In the following many-atom PIMC calculations, we choose 13 HF orbitals that are generated with 6-31G basis in Eq. 4.

B. Equation of state

Figure 4 shows the calculated internal energies and pressures along nine isochores relative to the ideal Fermi electron gas model⁸⁸. Our results show excellent agreement between PIMC and DFT-MD at 2×10^6 K for all densities. The difference between PIMC and DFT-MD is typically less than 3 Ha/atom in internal energy and within 3% in pressure. We have thus succeeded in constructing a coherent first-principles EOS table for warm dense sodium, over a wide range of densities (2-12 ρ_{ambient}) and temperatures (10^3 - 1.29×10^8 K).

At high temperatures of $T > 2 \times 10^7$ K, our PIMC results agree with those from the Debye-Hückel model as well as the Fermi electron gas theory, because the temperatures are so high that the atoms are fully ionized.

PIMC successfully bridges DFT-MD at 2×10^6 K and analytical models in the high-temperature limit. This cross-validates the EOS data from present PIMC simulations with fixed-node approximation, and the use of a frozen core and a zero-temperature exchange-correlation functional in DFT-MD up to 2×10^6 K.

As temperature decreases, the ideal Fermi electron gas model significantly overestimates the energy and the pressure because it neglects all interactions. This is partially improved in the Debye-Hückel model, which treats weak interactions correctly within the screening approximation. However, because the Debye-Hückel model still does not treat bound states, it leads to unphysically low pressures and energies at low temperatures, as the screening approximation breaks down and electrons occupy bound states.

In addition, Fig. 5 shows the nuclear pair-correlation functions $g_{\text{Na-Na}}(r)$ computed in DFT-MD and PIMC

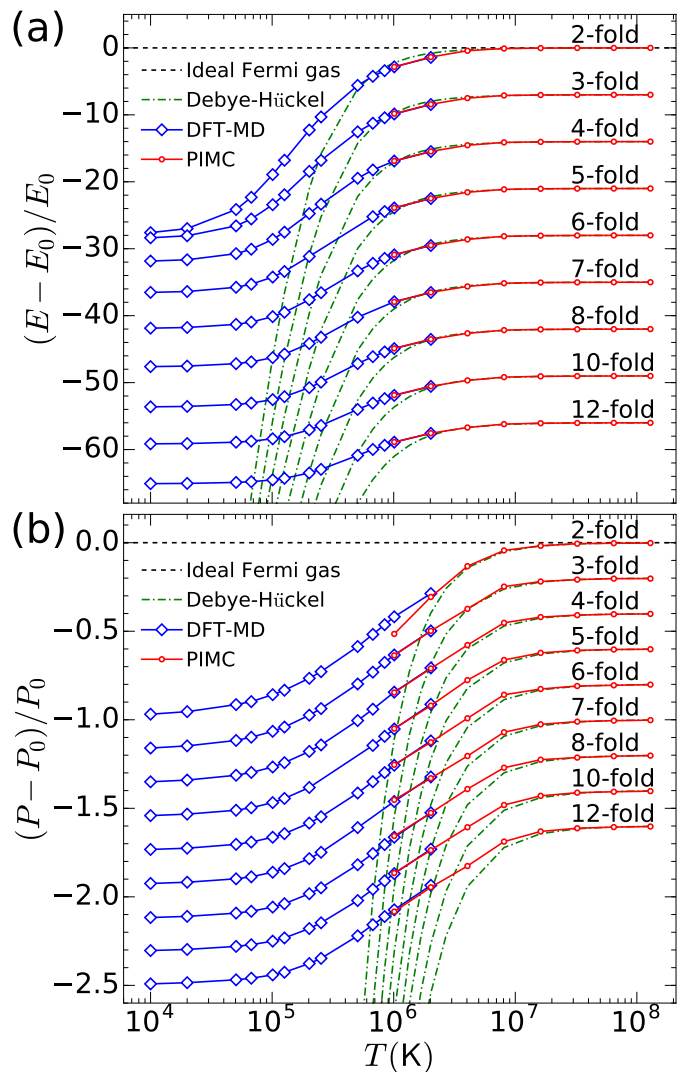


FIG. 4. Excess internal energies and pressures, relative to the ideal Fermi gas, for a 8-atom simulations along nine isochores (2, ..., 12-fold compression of ambient density). Corresponding results of the Debye-Hückel theory are plotted for comparison. For clarity, each energy curve at three-times-ambient or higher density is shifted by -7, and the pressure curve is shifted by -0.2, with respect to the nearby one with lower density. PIMC and DFT-MD predict consistent results at 2×10^6 K and PIMC agrees with analytical models at above 2×10^7 K.

simulations using an 8-atom simulation cell at 10^6 K and 8-fold compression. The good agreement in the $g_{\text{Na-Na}}(r)$ between the two methods shows that PIMC and DFT-MD predict consistent ionic plasma structures. This is further confirmation that the fixed-node approximation in PIMC and the exchange-correlation and pseudopotential approximation in DFT-MD do not inhibit the accuracy of these methods in the WDM regime.

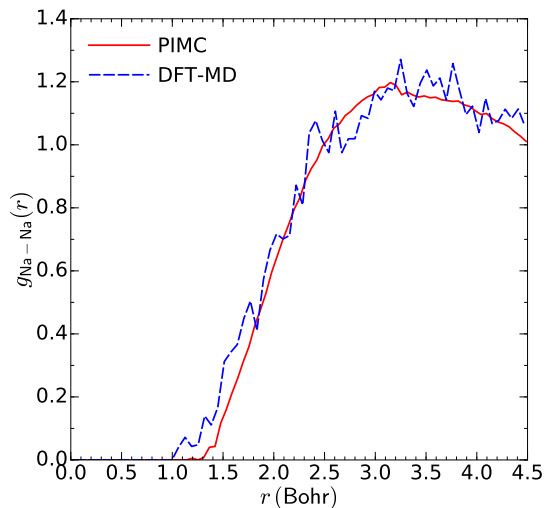


FIG. 5. Comparison of the nuclear pair correlation function obtained from DFT-MD and PIMC for 8-atom simulation cells at 10^6 K and under 8-fold compression.

C. Shock compression

In dynamic compression experiments, the conservation of mass, momentum, and energy constrains a steady shock to follow the Rankine-Hugoniot equation⁸⁹

$$\mathcal{H}(T, \rho) = (E - E_0) + \frac{1}{2}(P + P_0)(V - V_0) = 0, \quad (5)$$

where (E_0, P_0, V_0) and (E, P, V) represents the internal energy, pressure, and volume of the initial and the shocked state, respectively. The EOS (E and P on a grid of T and V) data in the previous section allows us to solve Eq. 5 with spline fitting.

Given that samples in shock experiments may be pre-compressed to reach higher-density, lower-temperature states off the principal Hugoniot, we consider four different initial conditions corresponding to 0.75, 1.0, 1.5, and 2.0 times ρ_{ambient} . DFT simulations are performed at each of these densities to determine the corresponding initial pressures and internal energies.

We thus calculate the Hugoniot curves and represent them with pressure-density plots in Fig. 6. Two compression peak maxima are predicted along each of the Hugoniot curves, one above 2×10^6 K and the other below 10^6 K. We tested different bivariate interpolation methods for the EOS grid in $\rho - T$ space and observed consistent compression curves. Small discrepancies (<0.1) in the compression minimum in between the two peaks is observed. We attribute this to the non-smoothness caused by the small differences between EOS values obtained by PIMC and DFT-MD at the corresponding pressure and temperature conditions.

For comparison, we consider two shock compression profiles predicted by SESAME⁹⁰, which is a tabular database for the thermodynamic properties of materials that is constructed by connecting available shock wave

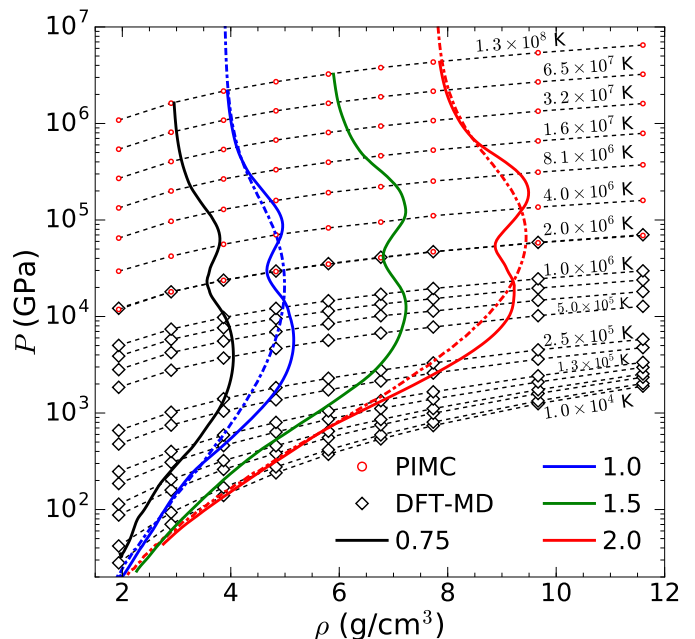


FIG. 6. Shock Hugoniot curves (solid curves) corresponding to four different initial densities 0.75, 1.0, 1.5, and 2 times ambient density represented in a pressure-density plot. Corresponding results from SESAME (dashed curves) at two initial densities are plotted for comparison. Isotherms are shown as black dashed lines.

data with Thomas-Fermi-Dirac and Mie-Grüneisen theory at high densities, and some simple analytic forms at low densities. The high-temperature limit is sufficiently described by the Thomas-Fermi-Dirac theory, as is shown by the remarkable consistency between the SESAME database and our present first-principles calculations at $T > 2 \times 10^7$ K. However, at lower temperatures when the system includes bound states, Fermi-Dirac breaks down and the SESAME database becomes insufficient. SESAME therefore fails to capture shell effects and only exhibits a single density peak along each Hugoniot curve.

Additionally, Fig. 7 shows temperature and pressure along the Hugoniot curve as functions of the shock compression ratio ρ/ρ_0 . When the initial density is the lowest ($\rho_0 = 0.75 \rho_{\text{ambient}}$), a maximum compression ratio of ~ 5.6 is reached at 6×10^5 K. The value of this peak decreases with increasing ρ_0 , and reduces to 4.7 when $\rho_0 = 2.0 \rho_{\text{ambient}}$. The higher-temperature compression peak reaches slightly larger compression ratio (4.9) than the lower peak as the initial density increases. In the high-temperature limit, the system is almost fully ionized and approaches the non-relativistic ideal limit ($\rho/\rho_0 = 4.0$), regardless of the initial density.

Figure 8 compares the principal Hugoniot curve of several elements including He⁵³, C⁴⁶, N⁵⁷, O⁵⁶, Ne⁵⁵, and Si⁴⁷. Interestingly, sodium together with helium show higher maximum compression ratio than other elements. We attribute this to the unusual low ambient density of sodium. In addition, each element imprints a particular

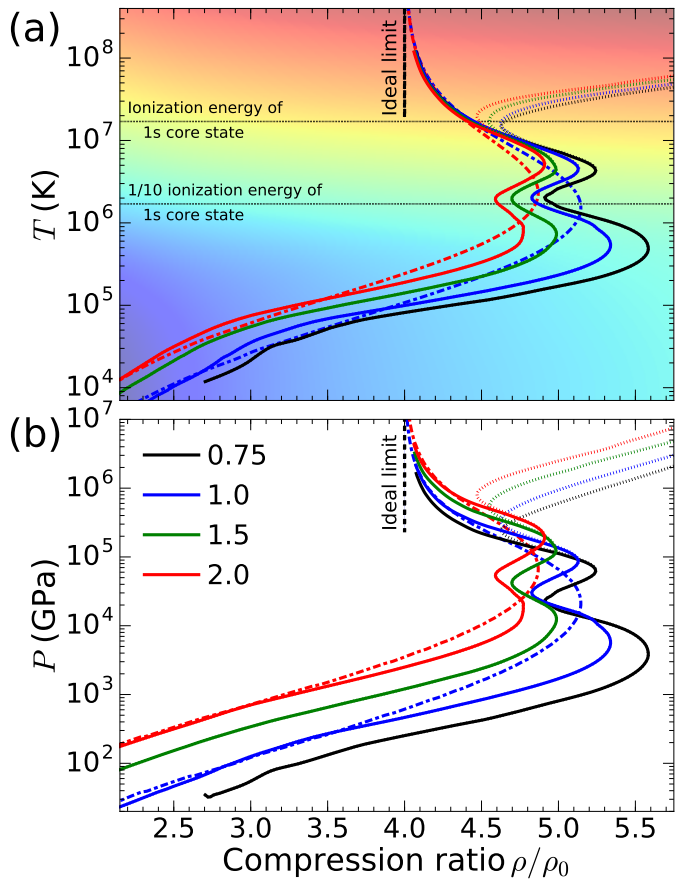


FIG. 7. Temperature and pressure as functions of the compression ratio along shock Hugoniot curves (solid curves) and those with radiation correction (dotted curves) corresponding to four initial densities 0.75, 1.0, 1.5, and 2 times ρ_{ambient} . Corresponding results from SESAME (dashed curves) at two initial densities are shown for comparison. The background color in the upper panel reflects the pressure changes.

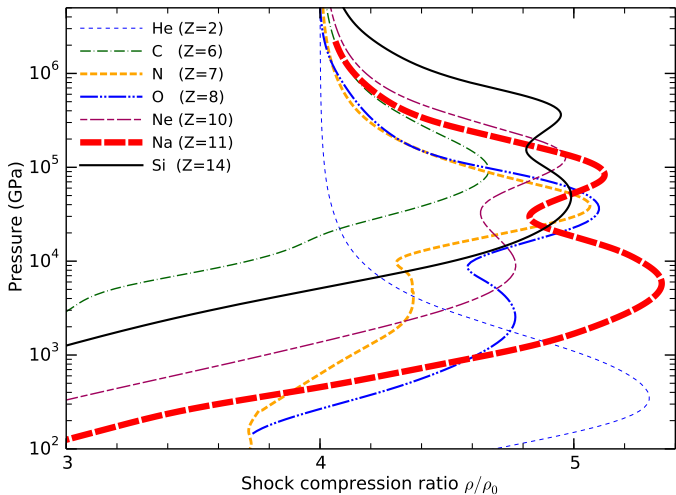


FIG. 8. The principal Hugoniot curve of sodium and other elements.

structural signature in its principal Hugoniot curve, exhibiting compression maxima with different values and at varied pressures and temperatures, due to the interplay of excitation of internal degrees of freedom, electronic interactions, and the interaction effects tied to the initial conditions⁷⁰.

Figure 1 compares the principal Hugoniot curve of sodium from our first-principles calculations and those predicted by widely-used EOS models, SESAME⁹⁰, LEOS^{91,92}, and average-atom Purgatorio (Lynx)^{93,94}. The compression maxima along the Hugoniot curves are closely related to ionization and interaction effects. SESAME and LEOS do not explicitly include information about electronic shell structure, and therefore do not show two distinct compression maxima. On the other hand, the DFT-based, average-atom Purgatorio (Lynx) model does compute the shell structure for an average of multiple ionization states. Therefore, Purgatorio (Lynx) agrees well with our first-principles results at above 200 GPa or 10^5 K. Below that, it is less reliable, because average-atom approaches cannot treat bonding and many body effects in a dense fluid properly. This is demonstrated by the deviation of the Hugoniot curve by Purgatorio (Lynx) from our calculations, which agrees with those predicted by SESAME and LEOS database, which were constructed by extrapolating experimental values.

We also compare our principal Hugoniot results with available experimental³²⁻³⁴ and theoretical^{41,43} data available at low temperatures and pressures. In comparison with the experimental data, the local pseudopotential theory⁴¹ underestimates the pressure by up to 30 GPa. The EAM model⁴³ agrees well with experiments up to 110 GPa, above which the model becomes invalid. Notably, DFT-MD, LEOS, and SESAME lie 10-20 GPa below the highest-pressure experimental data, but all methods tend to agree with the experimental data at the lowest pressures.

The shock velocity u_s and the particle velocity u_p that are of interests in shock experiments can be calculated using⁶⁴

$$u_s^2 = \xi/\eta \quad \text{and} \quad u_p^2 = \sqrt{\xi\eta}, \quad (6)$$

where $\xi = (P - P_0)/\rho_0$, $\eta = 1 - \rho_0/\rho$. Figure 9 compares the relation between u_s and u_p of sodium from our first-principles calculations and those predicted by the SESAME database, low-pressure ($P < 10^2$ GPa) shock experiments on sodium^{33,34}, and an “universal Hugoniot”⁹⁵ obtained from high-pressure (up to 0.2 Gbar) experimental Hugoniot data on Al, Fe, Cu, and Mo. We find the $u_s - u_p$ relation is well consistent with the linear relations predicted by experiments at $u_s < 15$ km/s^{33,34}, but increasingly deviates from them when the shock velocities exceeds ~ 500 km/s. This high velocity corresponds to a shock pressure of ~ 1.9 Gbar along the principal Hugoniot curve, and temperature of $\sim 10^7$ K, at which the atoms are nearly fully ionized (see the discussion in Sec. III D). The deviation from the “universal Hugoniot” of fluid metals⁹⁵ is more evident. This reflects

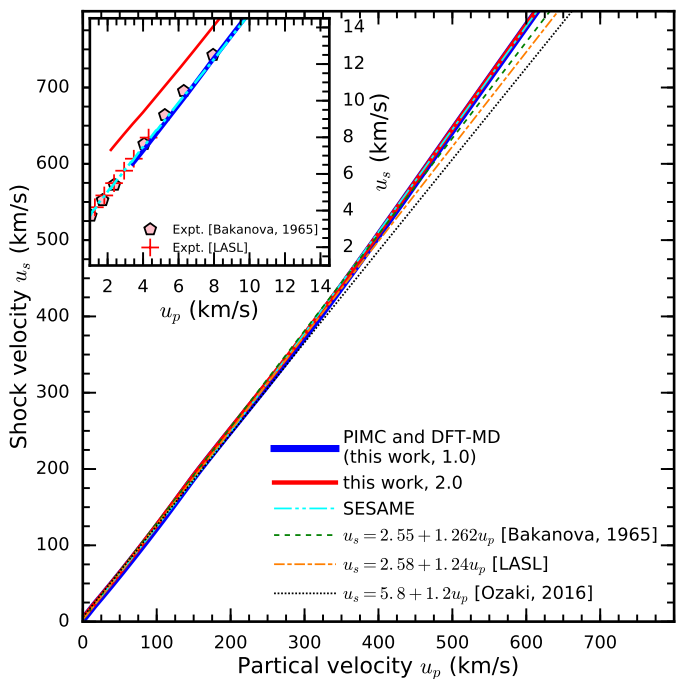


FIG. 9. $u_s - u_p$ diagram of sodium along two Hugoniot curves corresponding to initial densities of 1.0 and 2.0 times ambient density. The linear relations found in experiments are shown in dashed lines for comparison. The inset is a closer look at the low-velocity region. Shock pressures along the principal Hugoniot curve are ~ 1.9 Gbar at shock velocities near 500 km/s.

a fundamental difference between the effects of ionization on shock compression in sodium and in heavier metals, such as Fe, Cu, and Mo. The $u_s - u_p$ profile by SESAME agrees remarkably well with our first-principals predictions, which is not unexpected because of the nearly linear relation between u_s and u_p and the consistency between SESAME and our Hugoniot data at low ($< 10^4$ K) and high ($> 10^7$ K) temperature and pressure conditions (Figs. 6-7). Starting from pre-compressed sodium at 2 times ambient density, the shock velocity is higher but the slope du_s/du_p remains 1.31, according to linear interpolation.

When temperature exceeds 10^7 K, the radiation contribution becomes important. In order to evaluate the radiation effect on shock compression, we consider an ideal black body scenario and add the photon contribution to the EOS using

$$P_{\text{radiation}} = \frac{4\sigma}{3c}T^4 \text{ and } E_{\text{radiation}} = 3P_{\text{radiation}}V, \quad (7)$$

where σ is the Stefan-Boltzmann constant and c is the speed of light in vacuum. We then re-construct the Hugoniot curves and show them Figs. 1 and 7. We find that the two compression peaks remain unchanged as we include radiative effects. However, the Hugoniot curves deviate significantly from the classical limit above 10^7 K and tend towards a compression ratio asymptote of 7.

These results imply that the radiation contribution plays a significant role in the shock compression of materials at extreme temperatures ($T > 10^7$ K) and pressures ($P > 1$ Gbar). In comparison, the pressure-contribution from relativistic effects, included in the Purgatorio (Lynx) model is much smaller (Fig. 1).

D. Ionization

The structure of the Hugoniot curves observed in the previous section can be understood from the density-temperature dependence of the ionization process. In order to examine this relation, Fig. 10 shows the number of electrons near the nucleus for a given temperature and density, $N_{\text{Na}-e}(r)$, given by the formula

$$N(r) = \left\langle \frac{1}{N_I} \sum_{e,I} \theta(r - |\vec{r}_e - \vec{r}_I|) \right\rangle, \quad (8)$$

where the sum includes all electron-ion pairs and θ represents the Heaviside function.

The $N_{\text{Na}-e}(r)$ functions at two different densities and a series of temperatures are compared with ionization states of isolated sodium ions (calculated with GAMESS). The results show that $N_{\text{Na}-e}(r)$ decreases with T , indicating the gradual ionization of the atoms with temperature. The energy levels of the 1s electrons are much deeper than those of the outer-shell electrons, and therefore only become excited above 2×10^6 K. This indicates that the upper peaks on the Hugoniot curve in Figs. 6 and 7 are related to the excitation of the K -shell electrons, while the lower peaks correspond to the excitation of L -shell electrons.

IV. CONCLUSIONS

In this work, we construct a thermal density matrix with localized, HF orbitals to construct fermion nodal surfaces and perform PIMC simulations of the second-row element sodium. We obtain an accurate EOS from temperatures of 129 million to 1 million K, at which the results are consistent with DFT-MD. The excellent agreement between the PIMC and DFT-MD validates the use of the pseudopotential that freezes 1s electrons and the use of zero-temperature exchange-correlation functionals up to temperatures of 2×10^6 K.

By investigating the shock compression curves using the obtained EOS data, we find two compression maxima along the Hugoniot curves. This is in contrast to the single-peak Hugoniot curve predicted by the SESAME and the LEOS database, which are based on models that neglect bonding and many-body effects. The higher-temperature compression maxima occurs at 6×10^6 K due to the significant excitation of 1s electrons, while the lower compression maximum is due to the thermal excitation of outer-shell electrons. We predict a maximum

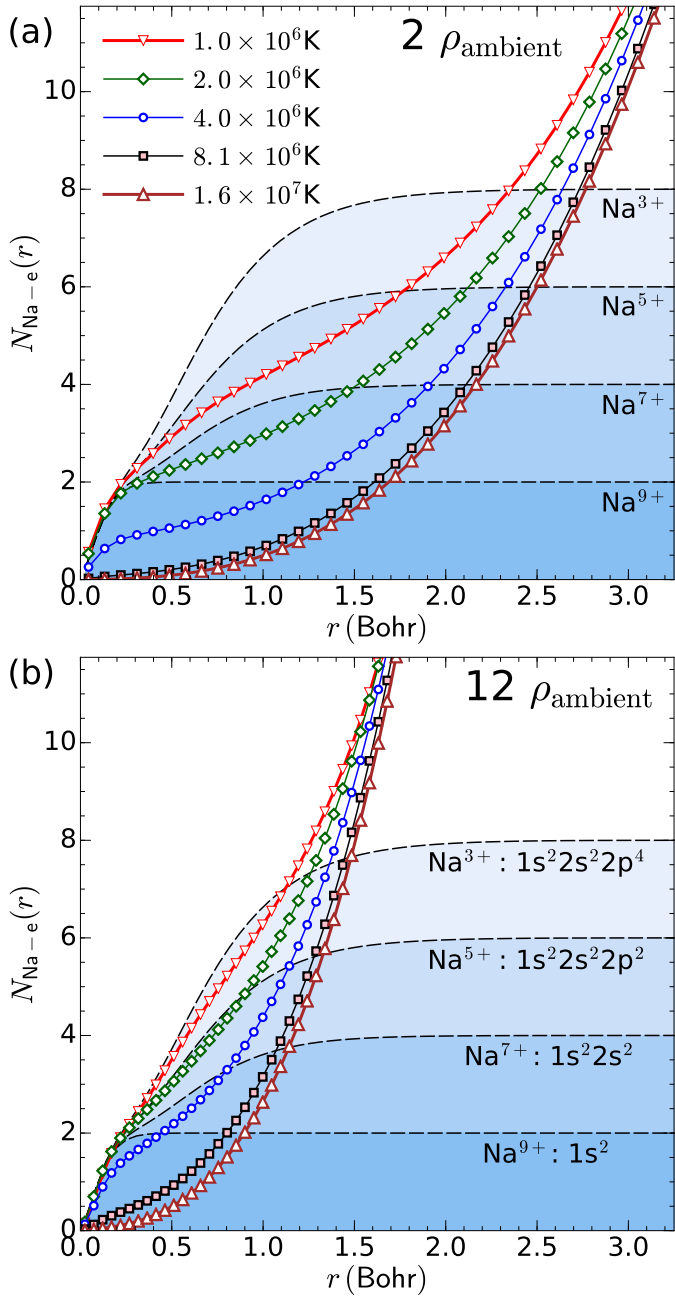


FIG. 10. Number of electrons near each nucleus at two densities ($\rho = 2$ and 12 times ρ_{ambient}) and a series of increasing temperatures. The profiles of four different ionization states of an isolated sodium atom, calculated with GAMESS), are shown for comparison.

compression ratio of 5.3 along the principal Hugoniot, and compression ratios of greater than 5 can be reached when the initial density is less than $1.5 \rho_{\text{ambient}}$. The value decreases at higher initial densities due to stronger particle interaction, and vice versa. Including a radiation contribution, shock Hugonits are modified significantly above 10^7 K and 1 Gbar and a much higher compression ratio can be reached.

V. SUPPLEMENTARY MATERIAL

See the supplementary material for the tables of EOS data.

ACKNOWLEDGMENTS

This research is supported by the U. S. Department of Energy, grant DE-SC0010517 and DE-SC0016248. Shuai Zhang is partially supported by the PLS-Postdoctoral Grant of the Lawrence Livermore National Laboratory. Computational support was provided by the Janus supercomputer, which is supported by the National Science Foundation (Grant No. CNS-0821794), the University of Colorado, and the National Center for Atmospheric Research, and NERSC. This research is part of the Blue Waters sustained-petascale computing project (NSF ACI 1640776), which is supported by the National Science Foundation (awards OCI-0725070 and ACI-1238993) and the state of Illinois. Blue Waters is a joint effort of the University of Illinois at Urbana-Champaign and its National Center for Supercomputing Applications. S.Z. appreciates the helpful discussion with Mu Li.

- ¹E. P. Wigner and F. Seitz, Phys. Rev. **43**, 804 (1933).
- ²J. Neaton and N. Ashcroft, Phys. Rev. Lett. **86**, 2830 (2001).
- ³M. Eremets, *High Pressure Experimental Methods Oxford Science Publications* (Oxford University Press, Oxford, 1996).
- ⁴L. Dubrovinsky, N. Dubrovinskaiia, V. B. Prakapenka, and A. M. Abakumov, Nature Commun. **3**, 1163 (2012).
- ⁵E. Gregoryanz, L. F. Lundegaard, M. I. McMahon, C. Guillaume, R. J. Nelmes, and M. Mezouar, Science **320**, 1054 (2008).
- ⁶I. Aleksandrov, V. Kachinskii, I. Makarenko, and S. Stishov, ZhETF Pisma Redaktsiiu **36**, 336 (1982).
- ⁷J. N. Fritz and B. Olinger, J. Chem. Phys. **80**, 2864 (1984).
- ⁸M. Hanfland, I. Loa, and K. Syassen, Phys. Rev. B **65**, 184109 (2002).
- ⁹J.-Y. Raty, E. Schwegler, and S. A. Bonev, Nature **449**, 448 (2007).
- ¹⁰M. I. McMahon, E. Gregoryanz, L. F. Lundegaard, I. Loa, C. Guillaume, R. J. Nelmes, A. K. Kleppe, M. Amboage, H. Wilhelm, and A. P. Jephcoat, Proc. Natl. Acad. Sci. USA **104**, 17297 (2007).
- ¹¹B. Rousseau, Y. Xie, Y. Ma, and A. Bergara, Eur. Phys. J. B **81**, 1 (2011).
- ¹²Y. Ma, M. Eremets, A. R. Oganov, Y. Xie, I. Trojan, S. Medvedev, A. O. Lyakhov, M. Valle, and V. Prakapenka, Nature **457**, 182 (2009).
- ¹³A. Lazicki, A. F. Goncharov, V. V. Struzhkin, R. E. Cohen, Z. Liu, E. Gregoryanz, C. Guillaume, H.-K. Mao, and R. J. Hemley, Proc. Natl. Acad. Sci. USA **106**, 6525 (2009).
- ¹⁴M. Gatti, I. V. Tokatly, and A. Rubio, Phys. Rev. Lett. **104**, 216404 (2010).
- ¹⁵H.-K. Mao, Y. Ding, Y. Xiao, P. Chow, J. Shu, S. Lebgue, A. Lazicki, and R. Ahuja, Proc. Natl. Acad. Sci. USA **108**, 20434 (2011).
- ¹⁶M. Marqués, M. Santoro, C. L. Guillaume, F. A. Gorelli, J. Contreras-García, R. T. Howie, A. F. Goncharov, and E. Gregoryanz, Phys. Rev. B **83**, 184106 (2011).
- ¹⁷I. Loa, K. Syassen, G. Monaco, G. Vankó, M. Krisch, and M. Hanfland, Phys. Rev. Lett. **107**, 086402 (2011).
- ¹⁸M. Pozzo, M. P. Desjarlais, and D. Alfé, Phys. Rev. B **84**, 054203 (2011).

- ¹⁹J. Ibañez Azpiroz, B. Rousseau, A. Eiguren, and A. Bergara, Phys. Rev. B **89**, 085102 (2014).
- ²⁰M.-s. Miao and R. Hoffman, J. Am. Chem. Soc. **137**, 3631 (2015).
- ²¹I. I. Naumov and R. J. Hemley, Phys. Rev. Lett. **114**, 156403 (2015).
- ²²E. Gregoryanz, O. Degtyareva, M. Somayazulu, R. J. Hemley, and H.-k. Mao, Phys. Rev. Lett. **94**, 185502 (2005).
- ²³L. Koči, R. Ahuja, L. Vitos, and U. Pinsook, Phys. Rev. B **77**, 132101 (2008).
- ²⁴A. Yamane, F. Shimojo, and K. Hoshino, J. Phys. Soc. Japan **77**, 064603 (2008).
- ²⁵E. G. Maksimov, S. V. Lepeshkin, and M. V. Magnitskaya, Crystallogr. Rep. **56**, 676 (2011).
- ²⁶H. Eshet, R. Z. Khaliullin, T. D. Kühne, J. Behler, and M. Parrinello, Phys. Rev. Lett. **108**, 115701 (2012).
- ²⁷D. J. González and L. E. González, AIP Conf. Proc. **1673**, 020005 (2015).
- ²⁸Y. Li, Y. Wang, C. J. Pickard, R. J. Needs, Y. Wang, and Y. Ma, Phys. Rev. Lett. **114**, 125501 (2015).
- ²⁹D. Swift, J. Hawreliak, D. Braun, A. Kritcher, S. Glenzer, G. W. Collins, S. Rothman, D. Chapman, and S. Rose, AIP Conf. Proc. **1426**, 477 (2012).
- ³⁰A. L. Kritcher, T. Doepfner, D. Swift, J. Hawreliak, J. Nilsen, J. Hammer, B. Bachmann, G. Collins, O. Landen, C. Keane, S. Glenzer, S. Rothman, D. Chapman, D. Kraus, and R. Falcone, J. Phys. Conf. Ser. **688**, 012055 (2016).
- ³¹A. A. Golyshev, D. V. Shakhrya, V. V. Kim, A. M. Molodets, and V. E. Fortov, Phys. Rev. B **83**, 094114 (2011).
- ³²M. H. Rice, J. Phys. Chem. Solids **26**, 483 (1965).
- ³³A. Bakanova, I. P. Dudoladov, and R. F. Trunin, Sov. Phys. Solid State **7**, 1307 (1965).
- ³⁴LASL Shock Hugoniot Data, edited by S. P. Marsh (University of California Press, Berkeley, 1980).
- ³⁵J. Ehrenfeld, S. Krimsky, and J. Selvitella, J. Appl. Phys. **37**, 4737 (1966).
- ³⁶D. P. Hickey, J. Appl. Phys. **38**, 4080 (1967).
- ³⁷D. J. Pastine, Phys. Rev. Lett. **18**, 1187 (1967).
- ³⁸D. J. Pastine, Phys. Rev. **166**, 703 (1968).
- ³⁹K. V. Khishchenko, J. Phys. Conf. Ser. **98**, 032023 (2008).
- ⁴⁰M. Ross, Phys. Rev. B **21**, 3140 (1980).
- ⁴¹D. A. Young and M. Ross, Phys. Rev. B **29**, 682 (1984).
- ⁴²D. K. Belashchenko, High Temp. **47**, 494 (2009).
- ⁴³D. K. Belashchenko, High Temp. **51**, 626 (2013).
- ⁴⁴D. K. Belashchenko, Phys. Usp. **56**, 1176 (2013).
- ⁴⁵C. Pierleoni, D. M. Ceperley, B. Bernu, and W. R. Magro, Phys. Rev. Lett. **73**, 2145 (1994).
- ⁴⁶K. P. Driver and B. Militzer, Phys. Rev. Lett. **108**, 115502 (2012).
- ⁴⁷B. Militzer and K. P. Driver, Phys. Rev. Lett. **115**, 176403 (2015).
- ⁴⁸S. X. Hu, B. Militzer, L. A. Collins, K. P. Driver, and J. D. Kress, Phys. Rev. B **94**, 094109 (2016).
- ⁴⁹F. Lambert and V. Recoules, Phys. Rev. E **86**, 026405 (2012).
- ⁵⁰C. Gao, S. Zhang, W. Kang, C. Wang, P. Zhang, and X. T. He, Phys. Rev. B **94**, 205115 (2016).
- ⁵¹S. Zhang, H. Wang, W. Kang, P. Zhang, and X. T. He, Phys. Plasmas **23**, 042707 (2016).
- ⁵²B. Militzer and D. M. Ceperley, Phys. Rev. E **63**, 066404 (2001).
- ⁵³B. Militzer, Phys. Rev. B **79**, 155105 (2009).
- ⁵⁴L. X. Benedict, K. P. Driver, S. Hamel, B. Militzer, T. Qi, A. A. Correa, A. Saul, and E. Schwegler, Phys. Rev. B **89**, 224109 (2014).
- ⁵⁵K. P. Driver and B. Militzer, Phys. Rev. B **91**, 045103 (2015).
- ⁵⁶K. P. Driver, F. Soubiran, S. Zhang, and B. Militzer, J. Chem. Phys. **143**, 164507 (2015).
- ⁵⁷K. P. Driver and B. Militzer, Phys. Rev. B **93**, 064101 (2016).
- ⁵⁸S. Zhang, K. P. Driver, F. Soubiran, and B. Militzer, High Energ. Dens. Phys. **21**, 16 (2016).
- ⁵⁹P. Debye and E. Huckel, Phys. Z. **24**, 185 (1923).
- ⁶⁰T. Sjostrom and J. Daligault, Phys. Rev. Lett. **113**, 155006 (2014).
- ⁶¹V. V. Karasiev, L. Calderín, and S. B. Trickey, Phys. Rev. E **93**, 063207 (2016).
- ⁶²R. P. Feynman, Phys. Rev. **91**, 1291 (1953).
- ⁶³W. R. Magro, D. M. Ceperley, C. Pierleoni, and B. Bernu, Phys. Rev. Lett. **76**, 1240 (1996).
- ⁶⁴B. Militzer, D. M. Ceperley, J. D. Kress, J. D. Johnson, L. A. Collins, and S. Mazevet, Phys. Rev. Lett. **87**, 275502 (2001).
- ⁶⁵S. X. Hu, B. Militzer, V. N. Goncharov, and S. Skupsky, Phys. Rev. Lett. **104**, 235003 (2010).
- ⁶⁶B. Militzer and D. M. Ceperley, Phys. Rev. Lett. **85**, 1890 (2000).
- ⁶⁷S. X. Hu, B. Militzer, V. N. Goncharov, and S. Skupsky, Phys. Rev. B **84**, 224109 (2011).
- ⁶⁸B. Militzer, W. Magro, and D. Ceperley, Contrib. Plasm. Phys. **39**, 151 (1999).
- ⁶⁹B. Militzer and R. L. Graham, J. Phys. Chem. Solids **67**, 2136 (2006).
- ⁷⁰B. Militzer, Phys. Rev. Lett. **97**, 175501 (2006).
- ⁷¹B. Militzer, J. Low Temp. Phys. **139**, 739 (2005).
- ⁷²B. Militzer and E. L. Pollock, Phys. Rev. B **71**, 134303 (2005).
- ⁷³E. L. Pollock and B. Militzer, Phys. Rev. Lett. **92**, 021101 (2004).
- ⁷⁴D. M. Ceperley, J. Stat. Phys. **63**, 1237 (1991).
- ⁷⁵S. A. Khairallah, J. Shumway, and E. W. Draeger, arXiv:1108.1711.
- ⁷⁶B. Militzer, Ph.D. Thesis, University of Illinois at Urbana-Champaign (2000).
- ⁷⁷B. Militzer, Comput. Phys. Commun. **204**, 88 (2016).
- ⁷⁸G. Kresse and J. Furthmüller, Phys. Rev. B **54**, 11169 (1996).
- ⁷⁹J. P. Perdew and A. Zunger, Phys. Rev. B **23**, 5048 (1981).
- ⁸⁰D. M. Ceperley and B. J. Alder, Phys. Rev. Lett. **45**, 566 (1980).
- ⁸¹P. E. Blöchl, O. Jepsen, and O. K. Andersen, Phys. Rev. B **49**, 16223 (1994).
- ⁸²We checked the inter-atomic distance and found that the 1.45-Bohr core radius and ~ 1.2 -Bohr projector cutoff radius defined in the pseudopotential are small enough to avoid core overlap at all densities up to 9.67 g/cm^3 ($10 \rho_{\text{ambient}}$). At 11.6 g/cm^3 ($12 \rho_{\text{ambient}}$), the cores of the nearest neighbors overlap by less than 0.2 Bohr, while the projectors do not overlap and the EOS data from DFT-MD still agree very well with PIMC values at 1 and 2 million K (within 1.6 Ha/atom in energy and 2% in pressure). Moreover, removing data at this density from the EOS table does not affect the Hugoniot curves nor does it matter for our discussion of the shock Hugoniot curves.
- ⁸³<http://opium.sourceforge.net>.
- ⁸⁴J. N. Bahcall and M. H. Pinsonneault, Phys. Rev. Lett. **92**, 121301 (2004).
- ⁸⁵Private communication with Cyril Georgy, University of Keele (United Kingdom).
- ⁸⁶J. P. Perdew, K. Burke, and M. Ernzerhof, Phys. Rev. Lett. **77**, 3865 (1996).
- ⁸⁷<http://www.msg.ameslab.gov/games/>.
- ⁸⁸Here, we include the kinetic energy of the nuclei when calculating the total internal energy of the ideal Fermi electron gas model, but have not considered the charge and interaction of the nuclei.
- ⁸⁹T. J. Ahrens, in *Encyclopedia of Geomagnetism and Paleomagnetism*, edited by D. Gubbins and E. Herrero-Bervera (Springer Netherlands, Dordrecht, 2003) pp. 912–920.
- ⁹⁰S. P. Lyon and J. D. Johnson, eds., *SESAME: The Los Alamos National Laboratory Equation of State Database* (Group T-1, Report No. LA-UR-92-3407, 1992).
- ⁹¹R. M. More, K. H. Warren, D. A. Young, and G. B. Zimmerman, Phys. Fluids **31**, 3059 (1988).
- ⁹²D. A. Young and E. M. Corey, J. Appl. Phys. **78**, 3748 (1995).
- ⁹³B. Wilson, V. Sonnad, P. Sterne, and W. Isaacs, J. Quant. Spectrosc. Radiat. Transfer **99**, 658 (2006).
- ⁹⁴H. D. Whitley and C. J. Wu, Lawrence Livermore National Laboratory Report No. LLNL-TR-705163 (2016).
- ⁹⁵N. Ozaki, W. J. Nellis, T. Mashimo, M. Ramzan, R. Ahuja, T. Kaewmaraya, T. Kimura, M. Knudson, K. Miyanishi, Y. Sakawa, T. Sano, and R. Kodama, Sci. Rep. **6**, 26000 (2016).